

Effect of structural water on the elasticity of orthopyroxene

MINGQIANG HOU^{1,†}, WEN-YI ZHOU^{1,2}, MING HAO^{1,2,‡}, FLORIAN TIAN-SIANG HUA³, JENNIFER KUNG³,
DONGZHOU ZHANG^{4,5}, PRZEMYSŁAW K. DERA⁴, AND JIN S. ZHANG^{1,2,*}

¹Institute of Meteoritics, University of New Mexico, Albuquerque, New Mexico 87131, U.S.A.

²Department of Earth and Planetary Sciences, University of New Mexico, Albuquerque, New Mexico 87131, U.S.A.

³Department of Earth Sciences, National Cheng-Kung University, Tainan City, Taiwan 701, Taiwan

⁴Hawai'i Institute of Geophysics and Planetology, University of Hawai'i at Mānoa, 1680 East-West Road, Honolulu, Hawaii 96822, U.S.A.

⁵Center of Advanced Radiation Sources, University of Chicago, Chicago, Illinois 60637, U.S.A.

ABSTRACT

As a major nominally anhydrous mineral (NAM) in the Earth's upper mantle, orthopyroxene could host up to several hundred parts per million H₂O in its crystal structure and transport the H₂O to the deep Earth. To study the effect of structural H₂O on the elasticity of orthopyroxene, we have measured the single-crystal elasticity of Mg_{1.991}Al_{0.065}Si_{1.951}O₆ with 842–900 ppm H₂O and 1.64 ± 0.20 wt% Al₂O₃ at ambient conditions using Brillouin spectroscopy. The best-fit single-crystal elastic moduli (C_{ij} s), bulk (K_{S0}), and shear (G_0) modulus of the hydrous Al-bearing orthopyroxene were determined as: $C_{11} = 235(2)$ GPa, $C_{22} = 173(2)$ GPa, $C_{33} = 222(2)$ GPa, $C_{44} = 86(1)$ GPa, $C_{55} = 82(1)$ GPa, $C_{66} = 82(1)$ GPa, $C_{12} = 75(3)$ GPa, $C_{13} = 67(2)$ GPa, and $C_{23} = 49(2)$ GPa, $K_{S0} = 111(2)$ GPa, and $G_0 = 78(1)$ GPa. Systematic analysis based on the results presented in this and previous studies suggests that the incorporation of 842–900 ppm H₂O would increase C_{13} by 12.0(7)% and decrease C_{23} by 8.6(8)%. The effects on C_{11} , C_{22} , C_{33} , C_{44} , C_{66} , K_{S0} , and V_P are subtle if not negligible when considering the uncertainties. The C_{55} , C_{12} , G_0 , and V_S are not affected by the presence of structural H₂O. Although laboratory experiments show that Fe,Al-bearing orthopyroxenes can host up to 0.8 wt% H₂O in its structure, future high-pressure-temperature elasticity measurements on orthopyroxene with higher H₂O content are needed to help better quantify this effect.

Keywords: Elasticity, orthopyroxene, structural water, seismic velocities

INTRODUCTION

Water, in the form of structural H₂O or free H₂O, is transported into the deep Earth's interior primarily via subduction. As an important carrier of structural H₂O, NAMs contain a small amount of H₂O in the form of hydroxyl as point defects in their crystalline structures (Demouchy and Bolfan-Casanova 2016; Ni et al. 2017; Ohtani 2005, 2015; Ohtani et al. 2004). The bonded structural H₂O can reach up to 1.2–3.1 wt% in the experimentally synthesized NAM crystals (Inoue et al. 1995; Kohlstedt et al. 1996). Moreover, a hydrous ringwoodite inclusion containing ~1.5 wt% H₂O was recently discovered in a natural diamond (Pearson et al. 2014), further highlighting the critical role that NAMs play as a possible major volatile reservoir in the deep Earth. Structural H₂O significantly impacts the ionic diffusion, dislocation motion, electrical conductivity, phase transitions, melting temperature, and viscosity of mantle minerals (Costa and Chakraborty 2008; Demouchy and Bolfan-Casanova 2016; Jacobsen et al. 2010; Yoshino et al. 2009; Zhang et al. 2012). In particular, recent studies have suggested that the presence of structural H₂O can result in some observable seismic signatures in the deep Earth (Kong et al. 2020; Van der Meijde et al. 2003; Yuan and Beghein 2013). Consequently, evaluating the effect of structural H₂O on the elastic properties of NAMs is crucial to

understand the seismic structure, volatile recycling, and mantle mineralogy in the deep Earth (e.g., Ni et al. 2017; Ohtani 2015; Ohtani et al. 2004).

The Earth's pyrolitic upper mantle is primarily composed of olivine, orthopyroxene, clinopyroxene, and garnet. The effects of structural H₂O on the elasticity of olivine and its high-pressure polymorphs have been extensively studied (Buchen et al. 2018; Inoue et al. 1998; Jacobsen et al. 2008; Kavner 2003; Mao et al. 2008, 2011, 2012; Schulze et al. 2018; Zhou et al. 2021, 2022). It was suggested that the presence of 1 wt% structural H₂O in the olivine polymorphs could reduce seismic velocities up to ~2.5% (Inoue et al. 1998; Jacobsen et al. 2008; Mao et al. 2008, 2011, 2012) and enhance the S-wave splitting anisotropy (Inoue et al. 1998; Jacobsen et al. 2008). However, recent studies showed that high pressure would suppress the effect of structural H₂O and the hydration-induced reductions of sound velocities vanish at transition zone pressure-temperature conditions (Buchen et al. 2018; Schulze et al. 2018; Zhou et al. 2021, 2022). Moreover, the effects of structural H₂O on the elastic properties of the Na,Al bearing-clinopyroxene, and garnet were found to be negligible at room-temperature condition (Fan et al. 2019; Mans et al. 2019). Although the orthorhombic orthopyroxene is the second most abundant mineral in the pyrolitic upper mantle, there has been no report about the effect of structural H₂O on its single-crystal elastic properties to date.

Compared with olivine, H₂O preferably partitions into orthopyroxene at depth above ~300 km in the upper mantle

* E-mail: jinzhang@unm.edu. Orcid 0000-0002-1936-7780

† Orcid 0000-0001-7003-3025

‡ Orcid 0000-0003-1380-3569

(Demouchy and Bolfan-Casanova 2016; Sakurai et al. 2014) and the incorporation of Al as chemical impurity enhances this partitioning process (Grant et al. 2006; Rauch and Keppler 2002; Smyth et al. 2007). There are two substitution mechanisms for structural H₂O in aluminous orthopyroxene. One is Al³⁺+H⁺ substitution for Si⁴⁺, and the other is Al³⁺+H⁺ substitution for 2 Mg²⁺. Laboratory-synthesized orthopyroxene crystals with high-Al₂O₃ content (9–12 wt%) can host up to ~0.8 wt% H₂O in its crystal structure (Mierdel et al. 2007), although natural orthopyroxenes commonly show lower H₂O concentration on the level of several hundred to 1000 ppm (Ohtani 2015; Xu et al. 2018).

Orthopyroxene presents the lowest isotropic aggregate compressional and shear velocities (v_p and v_s) among all major upper mantle minerals, and it has been proposed as a candidate to explain the low-seismic velocity zones in the upper mantle (Reynard et al. 2010). Single-crystal elastic properties of Al-, Fe-, and Ca-bearing orthopyroxene have been experimentally determined in a wide compositional range (Bass and Weidner 1984; Chai et al. 1997; Flesch et al. 1998; Jackson et al. 1999, 2007; Perrillat et al. 2007; Picek 2015; Qian et al. 2018; Reynard et al. 2010; Webb and Jackson 1993; Zhang et al. 2013; Zhang and Bass 2016). The incorporation of Fe significantly reduces the elastic moduli of orthopyroxene, whereas Al increases them (Picek 2015). The incorporation of Ca, on the other hand, slightly decreases the elastic properties of orthopyroxene (Perrillat et al. 2007). In this study, to evaluate the effect of structural H₂O on elastic properties of orthopyroxene, we conducted single-crystal Brillouin spectroscopy measurements of synthetic Al-bearing orthopyroxene with 842–900 ppm H₂O at ambient conditions.

MATERIALS AND METHODS

Hydrous Al-bearing orthopyroxene crystals were synthesized at 5.5 GPa and 1473 K using a multi-anvil press at National Cheng Kung University. Starting materials were oxide and hydroxide mixtures of SiO₂, MgO, Mg(OH)₂, and Al(OH)₃. Detailed synthesis method and procedure can be found in Hua et al. (2020). The size of the synthesized crystals ranges from 100 to 200 μm. The chemical composition of the crystals measured in this study was determined using a JEOL 8200 Electron Microprobe at the Institute of Meteoritics at the University of New Mexico, operating at 15 kV accelerating voltage and 20 nA beam current. The element standards were olivine for Mg and Si, enstatite oxygen standard for O, and orthoclase for Al. The determined chemical formula is: Mg_{1.991}Al_{0.065}Si_{1.951}O₆, with 39.82(43) wt% MgO, 58.18(73) wt% SiO₂, and 1.64(20) wt% Al₂O₃. The H₂O content was measured by SIMS technique and determined to be 842–900 ppm (Hua et al. 2020).

Three hydrous Al-bearing orthopyroxene crystals, which were examined to be inclusion-free under petrographic microscope, were selected and double-side polished with Al₂O₃ polishing film. The thicknesses of the samples were 18–20 μm. The orientations and unit-cell parameters were determined in the Atlas X-ray Diffraction Lab at the University of Hawai'i at Manoa, and the third one was measured at 13-BM-C, GeoSoilEnviroCARS (GSECARS), Advanced Photon Source, Argonne National Laboratory. The experimental setup and details can be found in Mans et al. (2019). The face normals of the three polished crystals are (0.940, -0.150, 0.307) (-0.566, 0.675, 0.472), and (-0.099, -0.558, -0.824), referring to the fractional coordinate system for orthopyroxene with unit-cell axes *a*, *b*, and *c* as basis vectors. The accuracy of the measured plane normal is better than 0.5°, which arises from the angular difference between the rotational axis of the DAC sample holder and the incident X-ray beam at the Atlas X-ray Diffraction Lab at University of Hawai'i and GSECARS sector13BMC. The unit-cell parameters [*a* = 5.175(3) Å, *b* = 8.804(7) Å, *c* = 18.216(3) Å, and *V* = 829.84(83) Å³] were determined by analyzing the X-ray diffraction images from all three samples, and the density was then calculated to be $\rho_0 = 3.218(3)$ g/cm³ using the chemical formula and unit-cell volume.

Brillouin spectroscopy measurements were conducted in the high-pressure laser spectroscopy laboratory at the University of New Mexico. A 300 mW single-mode diode-pumped solid-state laser with a wavelength (λ_0) of 532 nm was employed as

the light source. A Sandercock-type 6-pass tandem Fabry-Pérot interferometer was used for resolving the Brillouin frequency shift. The optical setup of the Brillouin spectroscopy system can be found in Zhang et al. (2015). All the experiments were conducted using a 50° symmetric forward scattering geometry. The scattering angle (θ) was calibrated to be 50.77(5)° before the experiments by a standard Corning 7980 silica glass, whose velocities have been precisely measured by the GHz ultrasound interferometry (Zhang et al. 2011). The sample crystal was placed on top of the culet of a diamond-anvil cell for Brillouin experiments. The tilting and non-parallelism of the sample and the diamond-anvil cell are negligible in the experiments. Under cross-polarized illumination of the petrographic microscope, the interference color of the double-side polished crystals is even, suggesting uniform thickness across the crystals. On the other hand, as part of the alignment process, we have also examined the tilting using the laser beam reflected at the diamond cutlets, tables, and crystal surfaces with 0° incident angle. The reflected laser beams match each other and the incident laser beam nicely, suggesting that the tilting is minimal. We calibrated the free spectral range (FSR) between the FP1 peaks under the reflection mode of the interferometer for at least six times before and after every experimental run, and the difference is always within 0.5 channels for a total of 1024-channel setup. This propagates to an uncertainty of <0.05% of the FSR and thus less than 0.005 km/s for each velocity measurement, which is within the resolution of Brillouin measurements of 0.03 km/s. The v_p and v_s were measured at 13 different χ angles (0°, 30°, 60°, 90°, 120°, 150°, 180°, 195°, 225°, 255°, 285°, 315°, 345°) for all three crystals along the 360° azimuth. The differences between determined velocities at $\chi = 0^\circ$ and $\chi = 180^\circ$ are within 0.05 km/s, again suggesting minimal geometrical errors in the experiments. The typical collection time for each spectrum is 10 min. Figure 1 shows a typical Brillouin spectrum and the signal-to-noise ratios are ~3 and ~7 for v_p and v_s , respectively.

Under a forward symmetric scattering geometry, the Brillouin shift $\Delta\omega$, which is the difference between incident laser frequency (ω_i) and scattered light frequency (ω_s), depends on the velocity along the probed phonon direction, the laser wavelength λ_0 , and the external experimental angle between the incident and the scattered light θ^* (Speziale et al. 2014; Whitfield et al. 1976; Zhang et al. 2015):

$$\Delta\omega = \omega_i - \omega_s = 2 \sin\left(\frac{\theta^*}{2}\right) \frac{v}{\lambda_0} \quad (1)$$

where v is the speed of the acoustic phonons in the sample.

The nine independent C_{ij} values can be calculated from the obtained v_p - v_s data set along different crystallographic directions by a least-squares inversion of the Christoffel equation (Weidner and Carleton 1977):

$$\det|c_{ijkl}n_jn_l - \rho v^2\delta_{ik}| = 0 \quad (2)$$

where c_{ijkl} is the fourth-order elasticity tensor, n_j and n_l are the directional cosines of the wave vector, ρ is density, and δ_{ik} is the Kronecker δ (Musgrave 1970). The predetermined plane normal by single-crystal X-ray diffraction was fixed during the inversion process. The angular uncertainty of <0.5° for the plane normal would

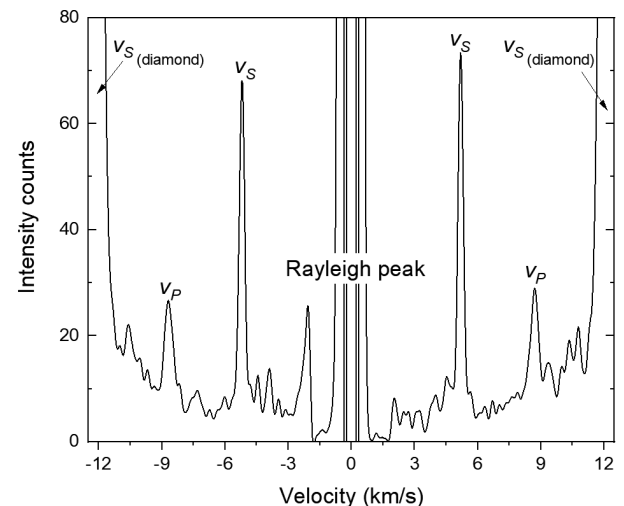


FIGURE 1. Representative Brillouin spectrum of the sample with plane normal (-0.566, 0.675, 0.472) measured at $\chi = 0^\circ$ for 10 min.

result in an uncertainty of <0.01 km/s in the measured acoustic velocities, which is well below the Brillouin measurement uncertainty of 0.03 km/s. However, we did refine the actual individual experimental phonon directions. Given a starting C_{ij} model of orthopyroxene (Zhang and Bass 2016), we calculated a set of phonon directions for each Brillouin measurement after fixing the plane normals. Then based on the phonon direction- v_p - v_s data set, we calculated the best-fit C_{ij} model through a least-square inversion of the Christoffel equation. Afterward, we then recalculate the phonon directions of each measurement based on this newly obtained best-fit C_{ij} model. The recalculated phonon directions and the velocities were used as the input to calculate an updated C_{ij} model for another round. This process was repeated for 2–3 times until the difference in root-mean-square (RMS) residuals of two successive runs was less than 0.001 km/s. The final best fit C_{ij} model we obtained has the RMS error of 0.055 km/s.

RESULTS

The best-fit C_{ij} values are: $C_{11} = 235(2)$ GPa, $C_{22} = 173(2)$ GPa, $C_{33} = 222(2)$ GPa, $C_{44} = 86(1)$ GPa, $C_{55} = 82(1)$ GPa, $C_{66} = 82(1)$ GPa, $C_{12} = 74(3)$ GPa, $C_{13} = 67(2)$ GPa, and $C_{23} = 49(2)$ GPa (Table 1). Figure 2 shows the measured acoustic velocities of the three crystals (Online Materials¹ Tables S1–S3) and the velocities predicted by the best-fit C_{ij} model. If the laboratory geometrical errors are negligible, the velocities of orthopyroxene measured at χ angle along the 360° azimuth should be the same as the velocities determined at χ -180°. Figure 2 plots the data measured at χ between 180–360° together with the data measured below 180°. The internal consistency between the data collected at (0°, 30°, 60°, 90°, 120°, 150°) and (180°, 195°, 225°, 255°, 285°, 315°, 345°) again suggests the minimal geometrical errors in this study. Voigt-Reuss-Hill (VRH) averaging scheme was employed to calculate the K_{S0} and G_0 (Hill 1963), which yielded 111(2) and 78(1) GPa, respectively. The aggregate V_p and V_s are calculated to be 8.18(3) and 4.94(2) km/s, respectively.

Our study demonstrates that the effects of Al₂O₃ and structural H₂O on the elasticity of orthopyroxene are coupled, and there is no existing study to quantify the contribution of Al₂O₃. The elastic properties of Fe-bearing orthopyroxene with Al₂O₃ content ranging from 0.4–5.0 wt% have been studied (Chai et al. 1997; Jackson et al. 2007; Webb and Jackson 1993; Zhang and Bass 2016). Decoupling the effects of Fe and Al₂O₃ is feasible

because the effect of Fe on the elasticity of orthopyroxene within a wide range of Fe# [Fe# = FeO/(FeO+MgO)] from 0–100 had been studied (Picek 2015). The C_{11} , C_{22} , C_{33} , C_{44} , C_{55} , and C_{66} of Fe-bearing orthopyroxene decrease with Fe#, whereas C_{12} , C_{13} , and C_{23} are insensitive to Fe#. To quantify the Al₂O₃ effect on the elastic properties of orthopyroxene, we would need to first evaluate the effect of Fe. Since the Fe# is <15 in the Al-bearing

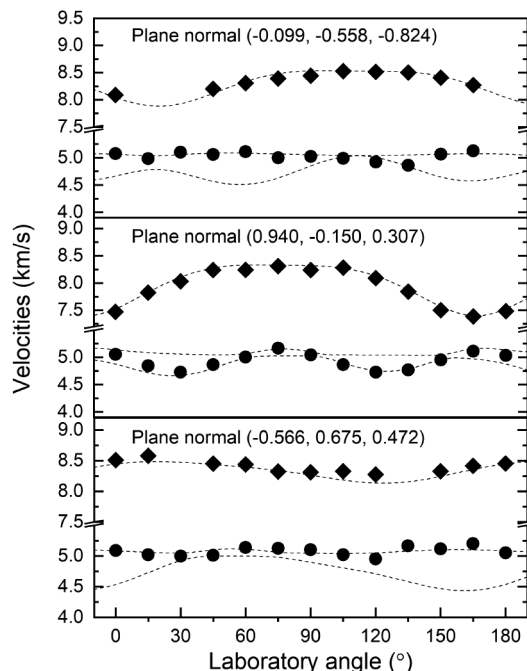


FIGURE 2. Acoustic velocities as a function of laboratory angle for the three hydrous Al-bearing orthopyroxene crystals. The solid diamonds and circles are measured v_p and v_s , respectively. Assigning the measured v_s as either v_{S1} or v_{S2} has negligible effect on the calculated C_{ij} model. The dashed curves are calculated from the best fit single-crystal C_{ij} model.

TABLE 1. The effect of chemical impurities on the elasticity of MgSiO₃ orthopyroxene

	Hydrous Al-bearing orthopyroxene (this study)	Al,Fe,Ca-bearing orthopyroxene (Zhang and Bass 2016)	Al,Fe,Ca-bearing orthopyroxene (Chai et al. 1997)	Al,Fe-bearing orthopyroxene (Jackson et al. 2007)	Ca-bearing orthopyroxene (Perrillat et al. 2007)	End-member orthopyroxene (Jackson et al. 1999)
H ₂ O (ppm)	842–900	–	–	–	0	0
Fe#	0	8.4	9.5	0.2	0	0
Al ₂ O ₃ (wt%)	1.64	2.5	5.0	0.4	0	0
CaO (wt%)	0	1.1	1.1	0	1.9	0
C_{11} (GPa)	235(2)	232.2(5)	236.9(10)	236(1)	224.1(1)	233(1)
C_{22} (GPa)	173(2)	175.7(7)	180.5(8)	173(1)	165.8(2)	171(1)
C_{33} (GPa)	222(2)	222.9(6)	230.4(10)	216(1)	202.9(1)	216(1)
C_{44} (GPa)	86(1)	82.2(4)	84.3(12)	84(1)	82.2(1)	83(1)
C_{55} (GPa)	82(1)	77.3(3)	79.4(8)	79(1)	73.8(1)	79(1)
C_{66} (GPa)	82(1)	78.1(6)	80.1(12)	80(1)	77.1(1)	77(1)
C_{12} (GPa)	75(3)	79.5(9)	79.6(16)	74(1)	71.4(1)	73(2)
C_{13} (GPa)	67(2)	61.2(6)	63.2(18)	57(1)	52.7(1)	56(2)
C_{23} (GPa)	49(2)	54.1(8)	56.8(24)	50(1)	45.2(1)	50(3)
ρ (g/cm ³)	3.218(3)	3.288(4)	3.304	3.196(4)	3.209	3.194(6)
$K_{S,Voigt}$ (GPa)	112(1)	113(1)	116.3(5)	109.5(15)	103.5(15)	108.7(15)
$G_{S,Voigt}$ (GPa)	79.1(5)	76.6(7)	78.6(4)	78.6(7)	74.9(11)	77.2(7)
$K_{S,Reuss}$ (GPa)	110(1)	112(1)	114.6(5)	107.4(15)	101.5(15)	106.7(15)
$G_{S,Reuss}$ (GPa)	77.7(5)	75.2(7)	77.3(4)	77.3(7)	73.5(11)	75.9(7)
$K_{S,VRH}$ (GPa)	111(2)	113(1)	115.5(5)	108.5(15)	102.5(15)	107.6(15)
$G_{S,VRH}$ (GPa)	78.4(1)	75.9(7)	78.1(4)	77.9(7)	74.2(11)	76.8(7)
V_p (km/s)	8.18(3)	8.06(3)	8.15(1)	8.15(8)	7.92	8.11
V_s (km/s)	4.94(2)	4.80(2)	4.86(1)	4.94(5)	4.81	4.90

orthopyroxene samples studied by Chai et al. (1997), Jackson et al. (2007), and Zhang and Bass (2016), we choose the data with the compositional range of interest for Fe# 0–15 in Picek (2015) together with previous studies (Jackson et al. 1999, 2007) to re-analyze the single-crystal elasticity data of Fe-bearing Al-free orthopyroxene. We found that increasing the Fe# by 1 would decrease C_{11} , C_{22} , C_{33} , C_{44} , C_{55} , and C_{66} by $-0.38(15)$, $-0.48(13)$, $-0.68(6)$, $-0.06(1)$, 0 , and $-0.10(1)$ GPa, respectively. On the other hand, there is ~ 1.1 wt% CaO in the Al,Fe-bearing orthopyroxene samples of Chai et al. (1997) and Zhang and Bass (2016). The effect of Ca on the elasticity of orthopyroxene had been carefully studied, and 1.1 wt% CaO would reduce the C_{11} , C_{22} , C_{33} , C_{44} , C_{55} , C_{66} , C_{12} , C_{13} , and C_{23} by 2.2, 1.7, 3.5, 0.56, 3.8, -0.75 , 2.1, 3.4, and 5.6%, respectively (Jackson et al. 1999; Perrillat et al. 2007).

After removing the effects of both Fe and Ca, we plotted the single-crystal and aggregate elastic moduli, as well as aggregate velocities of orthopyroxene as a function of Al_2O_3 content in Figure 3 (Online Materials¹ Table S4). The shaded area describes the effect of Al_2O_3 on the elasticity of orthopyroxene within the 95% confidence interval. The comparison between the data obtained in this study for hydrous Al-bearing orthopyroxene and previous anhydrous Al-bearing orthopyroxene in Figure 3 makes it possible to evaluate the effect of structural H_2O . The C_{11} , C_{22} , C_{33} of the hydrous Al-bearing orthopyroxene are 1.7(2), 3.0(1), and 2.1(4)% lower compared with its anhydrous counterparts, although the difference is subtle considering the experimental uncertainties. On the other hand, the decrease of C_{23} is more significant, up to 8.6(8)%. Interestingly, structural H_2O increases C_{44} , C_{66} , and C_{13} of the Al-bearing orthopyroxene by 2.6(3), 4.1(2), and 12.0(7)%, respectively. Structural H_2O has a negligible effect on C_{55} , C_{12} , K_{50} , G_0 , and V_s , although V_p is slightly decreased.

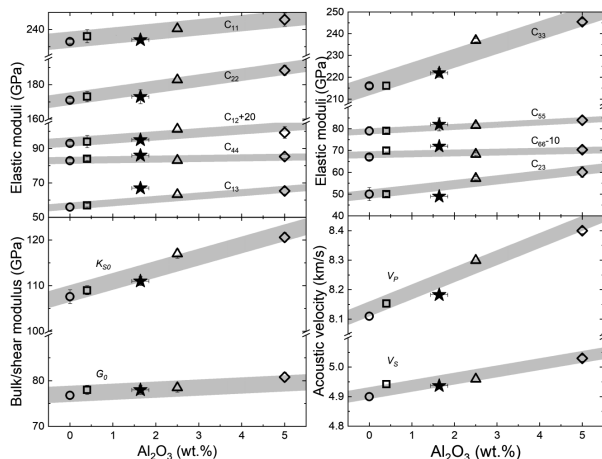


FIGURE 3. The effect of structural H_2O on the elasticity of orthopyroxene. The open circle, rectangle, triangle, and diamond symbols represent the elastic properties of anhydrous Al-bearing orthopyroxenes from Jackson et al. (1999, 2007), Zhang and Bass (2016), and Chai et al. (1997), respectively, after removing the Fe and Ca effects according to Picek (2015) and Perrillat et al. (2007). The shaded areas are bounded by the 95% confidence interval after linear-fitting. The solid star represents the data of hydrous Al-bearing orthopyroxene determined in this study. Most error bars are smaller than the symbols.

In addition, we also calculated the universal anisotropy (A^U), azimuthal V_p (A^{Vp}), and radial V_s anisotropy (D^{Vs}) of the hydrous Al-bearing orthopyroxene (Ranganathan and Ostoja-Starzewski 2008). A^U describes the overall elastic anisotropy for materials with arbitrary symmetry and can be calculated as follows:

$$A^U = 5 \frac{G_V}{G_R} + \frac{K_{SV}}{K_{S,R}} - 6 \quad (3)$$

where G and K_s are the shear and bulk moduli and the subscripts V and R represent Voigt and Reuss bound, respectively. A^{Vp} and D^{Vs} are the maximum v_p difference along different directions and maximum v_s difference between the two orthogonally polarized shear waves propagating along the same direction, respectively.

$$A^{Vp} = \frac{v_{p,\max} - v_{p,\min}}{V_{PVRH}} \quad (4)$$

$$D^{Vs} = \frac{|v_{s1} - v_{s2}|_{\max}}{V_{SVRH}} \quad (5)$$

The calculated anisotropy indices are 0.115(10), 0.148(6), and 0.153(6) and presented in Figure 4. With increasing the Al_2O_3 , A^U and A^{Vp} decrease, whereas D^{Vs} slightly increases. Compared with the anisotropy indices of anhydrous Al-bearing orthopyroxene, those of hydrous Al-bearing orthopyroxene seem higher, although the increase of D^{Vs} and A^{Vp} are too small to be considered significant. The A^U is most sensitive to the structural H_2O . 842–900 ppm H_2O increases the A^U by 14.4(30)%.

DISCUSSION AND IMPLICATIONS

Within the crystal structure of orthopyroxene, Si-O tetrahedra are connected by the bridging atom O3 to form chains extending along the c -axis, and the (Mg,Fe)-O octahedra are linked with

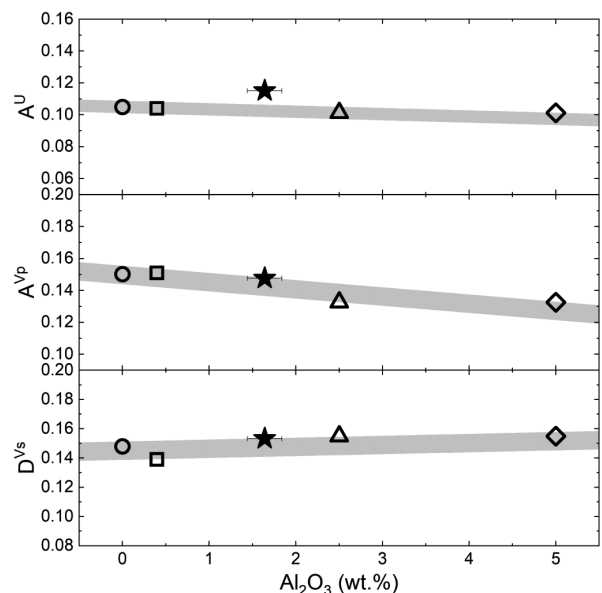


FIGURE 4. The effect of structural water on the A^U , A^{Vp} , and D^{Vs} of orthopyroxene. The symbols are the same as those in Figure 3.

each other through edge shearing (Online Materials¹ Fig. S1). The M1 and M2 sites are at the centers of edge-sharing octahedron and discontinuous octahedron, respectively. Compared to Mg, Fe prefers to occupy the slightly larger M2 site (Thompson and Downs 2003). As suggested by Duffy and Vaughan (1988) and Bass and Weidner (1984), the C_{11} , C_{22} , and C_{33} of anhydrous orthopyroxene are controlled by the stiffness of the M1, M2 octahedral sites and the compressibility of the Si-O tetrahedral chain, respectively. The shear elastic moduli C_{44} , C_{55} , and C_{66} are strongly affected by site ordering. Among them, C_{44} is more sensitive to composition and C_{55} and C_{66} are more sensitive to the octahedral stacking along a -axis. Finally, the off-diagonal elastic moduli C_{12} , C_{13} , and C_{23} vary slightly with either structure or composition. The substitution mechanism in hydrous orthopyroxene is dominated by the replacement of Si^{4+} with $\text{Al}^{3+}+\text{H}^+$ in the tetrahedral site or $\text{Al}^{3+}+\text{H}^+$ for 2Mg^{2+} in the M1 site (Mierdel et al. 2007). The reduction of C_{11} , C_{22} , and C_{33} caused by incorporation of 842–900 ppm structural H_2O is insignificant considering the uncertainties, suggesting that the substitution into the tetrahedral and octahedral sites does not induce a significant change in the compressibility along the a , b and c -axis. Among C_{44} , C_{55} , and C_{66} , C_{55} shows the least compositional variation (Duffy and Vaughan 1988). This is consistent with our observed increase of C_{44} and C_{66} yet negligible change in C_{55} as shown in Figure 3. The changes of the off-diagonal C_{ij} values such as C_{12} , C_{13} , and C_{23} observed in this study is difficult to be explained structurally, possibly related to the complicated effect caused by both the substitution of Al^{3+} into the tetrahedral site and the vacancies in the octahedral M1 and M2 sites introduced by hydration (Hua et al. 2020). Measurements of orthopyroxene with higher H_2O concentrations may provide further insight into the hydrogen induced elasticity variations.

Although 842–900 ppm structural H_2O has limited effect on the single-crystal elasticity of orthopyroxene, Mierdel et al. (2007) suggested that the incorporated structural H_2O could reach up to 0.8 wt% in the Fe-bearing orthopyroxene with high- Al_2O_3 contents. With such a high- H_2O content, the subtle decrease of V_p and increase of $D^{1/2}$ and $A^{1/2}$ can be more significant. In addition, the incorporation of Al and H_2O in orthopyroxene has an important effect on the development of deformation fabrics, which enhances the V_p anisotropy significantly (Manthilake et al. 2013). Considering the extremely high heterogeneity in the Earth's upper mantle and lower crust, the hydration effect in terms of seismic anisotropy can be important in the lithologies that are enriched in orthopyroxene, e.g., orthopyroxenite and pyroxenite (Arai et al. 2006; Smith et al. 1999), although future measurements at high pressure-temperature conditions on orthopyroxene with higher H_2O concentrations are needed to better quantify this effect.

FUNDING

This research was funded by NSF Grant EAR-1847707 (J.S.Z.) at the University of New Mexico. P.D. acknowledges support from NSF grant EAR-1722969.

REFERENCES CITED

- Arai, S., Shimizu, Y., Morishita, T., and Ishida, Y. (2006) A new type of orthopyroxenite xenolith from Takashima, Southwest Japan: silica enrichment of the mantle by evolved alkali basalt. *Contributions to Mineralogy and Petrology*, 152, 387–398.
- Bass, J.D., and Weidner, D.J. (1984) Elasticity of single-crystal orthoferrosilite. *Journal of Geophysical Research: Solid Earth*, 89, 4359–4371.
- Buchen, J., Marquardt, H., Speziale, S., Kawazoe, T., Ballaran, T.B., and Kurnosov, A. (2018) High-pressure single-crystal elasticity of wadsleyite and the seismic signature of water in the shallow transition zone. *Earth and Planetary Science Letters*, 498, 77–87.
- Chai, M., Brown, J.M., and Slutsky, L.J. (1997) The elastic constants of an aluminous orthopyroxene to 12.5 GPa. *Journal of Geophysical Research: Solid Earth*, 102, 14779–14785.
- Costa, F., and Chakraborty, S. (2008) The effect of water on Si and O diffusion rates in olivine and implications for transport properties and processes in the upper mantle. *Physics of the Earth and Planetary Interiors*, 166, 11–29.
- Demouchy, S., and Bolfan-Casanova, N. (2016) Distribution and transport of hydrogen in the lithospheric mantle: A review. *Lithos*, 240–243, 402–425.
- Duffy, T.S., and Vaughan, M.T. (1988) Elasticity of enstatite and its relationship to crystal structure. *Journal of Geophysical Research: Solid Earth*, 93, 383–391.
- Fan, D., Xu, J., Lu, C., Tkachev, S.N., Li, B., Ye, Z., Huang, S., Prakapenka, V.B., and Zhou, W. (2019) Elasticity of single-crystal low water content hydrous pyrope at high-pressure and high-temperature conditions. *American Mineralogist*, 104, 1022–1031.
- Flesch, L.M., Li, B., and Liebermann, R.C. (1998) Sound velocities of polycrystalline MgSiO_3 orthopyroxene to 10 GPa at room temperature. *American Mineralogist*, 83, 444–450.
- Grant, K.J., Kohn, S.C., and Brooker, R.A. (2006) Solubility and partitioning of water in synthetic forsterite and enstatite in the system $\text{MgO-SiO}_2\text{-H}_2\text{O-Al}_2\text{O}_3$. *Contributions to Mineralogy and Petrology*, 151, 651–664.
- Hill, R. (1963) Elastic properties of reinforced solids: some theoretical principles. *Journal of the Mechanics and Physics of Solids*, 11, 357–372.
- Hua, F.T.-S., Dera, P., and Kung, J. (2020) Compressional Behavior of Hydrous Orthoenstatite: Insight into the Nature of LVZ under Continental Plate. *Minerals*, 10, 71.
- Inoue, T., Yurimoto, H., and Kudoh, Y. (1995) Hydrous modified spinel, $\text{Mg}_{1.75}\text{SiH}_3\text{O}_4$: A new water reservoir in the mantle transition region. *Geophysical Research Letters*, 22, 117–120.
- Inoue, T., Weidner, D.J., Northrup, P.A., and Parise, J.B. (1998) Elastic properties of hydrous ringwoodite (γ -phase) in Mg_2SiO_4 . *Earth and Planetary Science Letters*, 160, 107–113.
- Jackson, J.M., Sinogeikin, S.V., and Bass, J.D. (1999) Elasticity of MgSiO_3 orthoenstatite. *American Mineralogist*, 84, 677–680.
- (2007) Sound velocities and single-crystal elasticity of orthoenstatite to 1073 K at ambient pressure. *Physics of the Earth and Planetary Interiors*, 161, 1–12.
- Jacobsen, S.D., Jiang, F., Mao, Z., Duffy, T.S., Smyth, J.R., Holl, C.M., and Frost, D.J. (2008) Effects of hydration on the elastic properties of olivine. *Geophysical Research Letters*, 35.
- Jacobsen, S.D., Liu, Z., Ballaran, T.B., Littlefield, E.F., Ehm, L., and Hemley, R.J. (2010) Effect of H_2O on upper mantle phase transitions in MgSiO_3 : Is the depth of the seismic X-discontinuity an indicator of mantle water content? *Physics of the Earth and Planetary Interiors*, 183, 234–244.
- Kavner, A. (2003) Elasticity and strength of hydrous ringwoodite at high pressure. *Earth and Planetary Science Letters*, 214, 645–654.
- Kohlstedt, D.L., Keppeler, H., and Rubie, D. (1996) Solubility of water in the α , β and γ phases of $(\text{Mg,Fe})_2\text{SiO}_4$. *Contributions to Mineralogy and Petrology*, 123, 345–357.
- Kong, F., Gao, S.S., Liu, K.H., Ding, W., and Li, J. (2020) Slab dehydration and mantle upwelling in the vicinity of the Sumatra Subduction Zone: Evidence from receiver function imaging of mantle transition zone discontinuities. *Journal of Geophysical Research: Solid Earth*, e2020JB019381.
- Mans, W., Zhang, J.S., Hao, M., Smyth, J.R., Zhang, D., Finkelstein, G.J., and Dera, P. (2019) Hydrogen Effect on the Sound Velocities of Upper Mantle Omphacite. *Minerals*, 9, 690.
- Manthilake, M., Miyajima, N., Heidelbach, F., Soustelle, V., and Frost, D.J. (2013) The effect of aluminum and water on the development of deformation fabrics of orthopyroxene. *Contributions to Mineralogy and Petrology*, 165, 495–505.
- Mao, Z., Jacobsen, S., Jiang, F., Smyth, J., Holl, C., and Duffy, T. (2008) Elasticity of hydrous wadsleyite to 12 GPa: Implications for Earth's transition zone. *Geophysical Research Letters*, 35.
- Mao, Z., Jacobsen, S.D., Frost, D.J., McCammon, C.A., Hauri, E.H., and Duffy, T.S. (2011) Effect of hydration on the single-crystal elasticity of Fe-bearing wadsleyite to 12 GPa. *American Mineralogist*, 96, 1606–1612.
- Mao, Z., Lin, J.-F., Jacobsen, S.D., Duffy, T.S., Chang, Y.-Y., Smyth, J.R., Frost, D.J., Hauri, E.H., and Prakapenka, V.B. (2012) Sound velocities of hydrous ringwoodite to 16 GPa and 673 K. *Earth and Planetary Science Letters*, 331–332, 112–119.
- Mierdel, K., Keppeler, H., Smyth, J.R., and Langenhorst, F. (2007) Water solubility in aluminous orthopyroxene and the origin of Earth's asthenosphere. *Science*, 315, 364–368.
- Momma, K., and Izumi, F. (2011) VESTA 3 for three-dimensional visualization of crystal, volumetric and morphology data. *Journal of Applied Crystallography*, 44, 1272–1276.

- Musgrave, M.J.P. (1970) *Crystal Acoustics: Introduction to the Study of Elastic Waves and Vibrations in Crystals*. [Acoustical Society of America, pp 621.
- Ni, H., Zheng, Y.-F., Mao, Z., Wang, Q., Chen, R.-X., and Zhang, L. (2017) Distribution, cycling and impact of water in the Earth's interior. *National Science Review*, 4, 879–891.
- Ohtani, E. (2005) Water in the mantle. *Elements*, 1, 25–30.
- (2015) Hydrous minerals and the storage of water in the deep mantle. *Chemical Geology*, 418, 6–15.
- Ohtani, E., Litasov, K., Hosoya, T., Kubo, T., and Kondo, T. (2004) Water transport into the deep mantle and formation of a hydrous transition zone. *Physics of the Earth and Planetary Interiors*, 143–144, 255–269.
- Pearson, D.G., Brenker, F.E., Nestola, F., McNeill, J., Nasdala, L., Hutchison, M.T., Matveev, S., Mather, K., Silversmit, G., Schmitz, S., Vekemans, B., and Vinze, L. (2014) Hydrous mantle transition zone indicated by ringwoodite included within diamond. *Nature*, 507, 221–224.
- Perrillat, J.P., Nestola, F., Sinogeikin, S.V., and Bass, J.D. (2007) Single-crystal elastic properties of Ca_{0.07}Mg_{1.93}Si₂O₆ orthopyroxene. *American Mineralogist*, 92, 109–113.
- Picek, S. M. (2015). Sound velocity study of natural orthopyroxenes with varying iron content. Master Thesis, University of Illinois at Urbana-Champaign. <https://www.ideals.illinois.edu/handle/2142/78756>.
- Qian, W., Wang, W., Zou, F., and Wu, Z. (2018) Elasticity of orthoenstatite at high pressure and temperature: Implications for the origin of low V_P/V_S zones in the mantle wedge. *Geophysical Research Letters*, 45, 665–673.
- Ranganathan, S.I., and Ostoja-Starzewski, M. (2008) Universal elastic anisotropy index. *Physical Review Letters*, 101, 055504.
- Rauch, M., and Keppler, H. (2002) Water solubility in orthopyroxene. *Contributions to Mineralogy and Petrology*, 143, 525–536.
- Reynard, B., Bass, J.D., and Brenizer, J. (2010) High-temperature elastic softening of orthopyroxene and seismic properties of the lithospheric upper mantle. *Geophysical Journal International*, 181, 557–566.
- Sakurai, M., Tsujino, N., Sakuma, H., Kawamura, K., and Takahashi, E. (2014) Effects of Al content on water partitioning between orthopyroxene and olivine: Implications for lithosphere–asthenosphere boundary. *Earth and Planetary Science Letters*, 400, 284–291.
- Schulze, K., Marquardt, H., Kawazoe, T., Boffa Ballaran, T., McCammon, C., Koch-Müller, M., Kurnosov, A., and Marquardt, K. (2018) Seismically invisible water in Earth's transition zone? *Earth and Planetary Science Letters*, 498, 9–16.
- Smith, D., Riter, J.A., and Mertzman, S.A. (1999) Water–rock interactions, orthopyroxene growth, and Si-enrichment in the mantle: evidence in xenoliths from the Colorado Plateau, southwestern United States. *Earth and Planetary Science Letters*, 165, 45–54.
- Smyth, J.R., Mierdel, K., Keppler, H., Langenhorst, F., Dubrovinsky, L., and Nestola, F. (2007) Crystal chemistry of hydration in aluminous orthopyroxene. *American Mineralogist*, 92, 973–976.
- Speziale, S., Marquardt, H., and Duffy, T.S. (2014) Brillouin scattering and its application in geosciences. *Reviews in Mineralogy and Geochemistry*, 78, 543–603.
- Thompson, R.M., and Downs, R.T. (2003) Model pyroxenes I: Ideal pyroxene topologies. *American Mineralogist*, 88, 653–666.
- Van der Meijde, M., Marone, F., Giardini, D., and Van der Lee, S. (2003) Seismic evidence for water deep in Earth's upper mantle. *Science*, 300, 1556–1558.
- Webb, S.L., and Jackson, I. (1993) The pressure dependence of the elastic moduli of single-crystal orthopyroxene (Mg_{0.8}Fe_{0.2})SiO₃. *European Journal of Mineralogy*, 5, 1111–1120.
- Weidner, D.J., and Carleton, H.R. (1977) Elasticity of coesite. *Journal of Geophysical Research*, 82, 1334–1346.
- Whitfield, C.H., Brody, E.M., and Bassett, W.A. (1976) Elastic moduli of NaCl by Brillouin scattering at high pressure in a diamond anvil cell. *Review of Scientific Instruments*, 47, 942–947.
- Xu, J., Zhang, D., Fan, D., Zhang, J.S., Hu, Y., Guo, X., (2018) Phase transitions in orthoenstatite and subduction zone dynamics: Effects of water and transition metal ions. *Journal of Geophysical Research: Solid Earth*, 123, 2723–2737.
- Yoshino, T., Matsuzaki, T., Shatskiy, A., and Katsura, T. (2009) The effect of water on the electrical conductivity of olivine aggregates and its implications for the electrical structure of the upper mantle. *Earth and Planetary Science Letters*, 288, 291–300.
- Yuan, K., and Beghein, C. (2013) Seismic anisotropy changes across upper mantle phase transitions. *Earth and Planetary Science Letters*, 374, 132–144.
- Zhang, J.S., and Bass, J.D. (2016) Single-crystal elasticity of natural Fe-bearing orthoenstatite across a high-pressure phase transition. *Geophysical Research Letters*, 43, 8473–8481.
- Zhang, J.S., Bass, J.D., Taniguchi, T., Goncharov, A.F., Chang, Y.-Y., and Jacobsen, S.D. (2011) Elasticity of cubic boron nitride under ambient conditions. *Journal of Applied Physics*, 109, 063521.
- Zhang, B., Yoshino, T., Wu, X., Matsuzaki, T., Shan, S., and Katsura, T. (2012) Electrical conductivity of enstatite as a function of water content: implications for the electrical structure in the upper mantle. *Earth and Planetary Science Letters*, 357–358, 11–20.
- Zhang, D., Jackson, J.M., Chen, B., Sturhahn, W., Zhao, J., Yan, J., and Caracas, R. (2013) Elasticity and lattice dynamics of enstatite at high pressure. *Journal of Geophysical Research: Solid Earth*, 118, 4071–4082.
- Zhang, J.S., Bass, J.D., and Zhu, G. (2015) Single-crystal Brillouin spectroscopy with CO₂ laser heating and variable q. *The Review of Scientific Instruments*, 86, 063905.
- Zhou, W.-Y., Ren, Z., Zhang, J.S., Chen, B., Hao, M., Ohuchi, T., Miyagi, L., Zhang, D., and Schmandt, B. (2021) The H₂O-Fe#-Pressure dependent single-crystal elastic properties of wadsleyite: Implications for the seismic anisotropy in the upper Mantle Transition Zone. *Earth and Planetary Science Letters*, 565, 116955.
- Zhou, W.-Y., Zhang, J.S., Huang, Q., Lai, X., Chen, B., Dera, P., Schmandt, B. (2022) High pressure-temperature single-crystal elasticity of ringwoodite: Implications for detecting the 520 discontinuity and metastable ringwoodite at depths greater than 660 km. *Earth and Planetary Science Letters*, 579, 117359.

MANUSCRIPT RECEIVED OCTOBER 7, 2020

MANUSCRIPT ACCEPTED APRIL 12, 2021

MANUSCRIPT HANDLED BY SERGIO SPEZIALE

Endnote:

¹Deposit item AM-22-47843, Online Materials. Deposit items are free to all readers and found on the MSA website, via the specific issue's Table of Contents (go to http://www.minsocam.org/MSA/AmMin/TOC/2022/Apr2022_data/Apr2022_data.html).